

## Electrochemistry

How to cite:

International Edition: doi.org/10.1002/anie.202003972

German Edition: doi.org/10.1002/ange.202003972

## Realizing Complete Solid-Solution Reaction in High Sodium Content P2-Type Cathode for High-Performance Sodium-Ion Batteries

Ting Jin<sup>†</sup>, Peng-Fei Wang<sup>†</sup>, Qin-Chao Wang, Kunjie Zhu, Tao Deng, Jiaxun Zhang, Wei Zhang, Xiao-Qing Yang, Lifang Jiao,\* and Chunsheng Wang\*

**Abstract:** P2-type layered oxides suffer from an ordered Na<sup>+</sup>/vacancy arrangement and P2→O2/OP4 phase transitions, leading them to exhibit multiple voltage plateaus upon Na<sup>+</sup> extraction/insertion. The deficient sodium in the P2-type cathode easily induces the bad structural stability at deep desodiation states and limited reversible capacity during Na<sup>+</sup> de/insertion. These drawbacks cause poor rate capability and fast capacity decay in most P2-type layered oxides. To address these challenges, a novel high sodium content (0.85) and plateau-free P2-type cathode-Na<sub>0.85</sub>Li<sub>0.12</sub>Ni<sub>0.22</sub>Mn<sub>0.66</sub>O<sub>2</sub> (P2-NLNMO) was developed. The complete solid-solution reaction over a wide voltage range ensures both fast Na<sup>+</sup> mobility (10<sup>-11</sup> to 10<sup>-10</sup> cm<sup>2</sup> s<sup>-1</sup>) and small volume variation (1.7%). The high sodium content P2-NLNMO exhibits a higher reversible capacity of 123.4 mAh g<sup>-1</sup>, superior rate capability of 79.3 mAh g<sup>-1</sup> at 20 C, and 85.4% capacity retention after 500 cycles at 5 C. The sufficient Na and complete solid-solution reaction are critical to realizing high-performance P2-type cathodes for sodium-ion batteries.

## Introduction

Sodium-ion batteries (SIBs) have been regarded as potential large-scale energy storage devices because of the wide distribution and low cost of sodium resources.<sup>[1]</sup> However, the performance of SIBs is still limited by sluggish Na kinetics and unsatisfactory energy density of the cathodes.<sup>[2]</sup> Similar to lithium-ion batteries, layered transition-metal oxides (Na<sub>x</sub>TMO<sub>2</sub>, TM represents transition metal, such as: Fe, Co, Mn, Ni, Cu, etc.) are the most promising cathodes because of their high theoretical specific capacity, low cost,

and facile synthesis.<sup>[3]</sup> Sodium-based layered compounds can be classified into two main groups: O3-type and P2-type.<sup>[4]</sup> Owing to the open prismatic paths and direct Na-ion diffusion between transition-metal layers for the P2 phase, P2-type compounds possess better structure stability than the O3 counterpart upon Na ion extraction and insertion processes. Nevertheless, the deficient Na content and multiple phase transitions upon charging/discharging still make P2-type layered oxides difficult for realizing the practical application.<sup>[5]</sup> The Na-deficient P2-Na<sub>x</sub>TMO<sub>2</sub> (*x* is usually ranged from 0.5 to 0.7) layered oxides normally delivers a low reversible capacity, thus leading to unsatisfactory energy density. Furthermore, once being charged to a high-voltage region, TMO<sub>2</sub> layers are inclined to slide and trigger the phase transition of P2→O2/OP4 as less Na remains in the NaO<sub>2</sub> layer.<sup>[6]</sup> The irreversible P2→O2 phase transition generates a large volume change of 23% and reduces the Na diffusivity because the diffusion energy barrier in the O2 phase is much larger than in the P2 phase.<sup>[7]</sup> Although the transition from P2 to OP4 is relatively reversible, the moderate structure variation still affects the battery performance at high rates. In addition, P2-type layered oxides experience complex Na<sup>+</sup>/vacancy ordering rearrangements below 4.0 V. The Na<sup>+</sup>/vacancy ordering rearrangement is induced by the large difference in ionic radii and small difference in Fermi level of transition metal, which is related to the Na diffusion within TMO<sub>2</sub> slabs.<sup>[8]</sup> Therefore, the fast capacity decay and slow Na<sup>+</sup> mobility can be induced by both phase transition from P2 to O2/OP4 and Na<sup>+</sup>/vacancy ordering in P2-type layered oxides. In previous studies, limiting the charge voltage to below 4.0 V and doping various cations (Mg<sup>2+</sup>,<sup>[9]</sup> Ti<sup>4+</sup>,<sup>[10]</sup> Li<sup>+</sup>,<sup>[11]</sup> Zn<sup>2+</sup>,<sup>[12]</sup> Cu<sup>2+</sup>,<sup>[13]</sup> etc.) in the transition metal (TM) sites are commonly adopted to delay and relieve the irreversible P2→O2 transition and Na<sup>+</sup>/vacancy ordering, yet at the expense of reversible capacity and operating voltage. And most of these strategies have not completely eliminated phase transitions. Therefore, increasing the Na content and fabricating complete solid-solution reactions for a wide voltage range are very important to improving the performance of P2-type layered oxides.

In this context, a high sodium content P2-type layered oxide of Na<sub>0.85</sub>Li<sub>0.12</sub>Ni<sub>0.22</sub>Mn<sub>0.66</sub>O<sub>2</sub> (P2-NLNMO) was designed for the first time. The smaller ionic radii ratio among Li<sup>+</sup> (76 pm), Ni<sup>2+</sup> (69 pm), and Mn<sup>4+</sup> (53 pm), not only effectively inhibit the Na<sup>+</sup>/vacancy ordering and charge ordering after the introduction of Li into the transition-metal layer, but also suppress the gliding of TM layers (that is: P2→O2 transition) in the deeply desodiated structure. The Na content as high as

[\*] T. Jin,<sup>[†]</sup> K. Zhu, Prof. W. Zhang, Prof. L. Jiao  
Key Laboratory of Advanced Energy Materials Chemistry (Ministry of Education), Renewable Energy Conversion and Storage Center (ReCast), College of Chemistry, Nankai University  
Tianjin 300071 (China)  
E-mail: jiaolf@nankai.edu.cn

T. Jin,<sup>[†]</sup> Dr. P.-F. Wang,<sup>[†]</sup> T. Deng, J. Zhang, Prof. C. Wang  
Department of Chemical and Biomolecular Engineering, University of Maryland, College Park, MD 20742 (USA)  
E-mail: cswang@umd.edu

Dr. Q.-C. Wang, Prof. X.-Q. Yang  
Chemistry Division, Brookhaven National Laboratory  
Upton, NY 11973 (USA)

[†] These authors contributed equally to this work.

Supporting information and the ORCID identification number(s) for the author(s) of this article can be found under:  
https://doi.org/10.1002/anie.202003972.



0.85 provides sufficient sodium reservoir for (de)intercalation without sacrificing the specific capacity. As a comparison, the Li-free compound of  $\text{Na}_{0.85}\text{Ni}_{0.34}\text{Mn}_{0.66}\text{O}_2$  (P2-NNMO) was also investigated. The thermodynamic stability of P2-NLNMO (versus O3-NLNMO) at a high Na content of 0.85 were confirmed through DFT calculations. The charge/discharge profiles of P2-NLNMO are sloping over the potential range of 2.0–4.3 V and the  $\text{Ni}^{2+}/\text{Ni}^{4+}$  redox chemistry is demonstrated as evidenced by X-ray absorption spectra (XAS). In situ X-ray diffraction (XRD) characterization confirms an absolute solid-solution reaction with a very small volume variation before and after extraction. The combined analysis of galvanostatic intermittent titration technique (GITT) and density-functional theory (DFT) calculations suggest fast  $\text{Na}^+$  diffusion and low migration barrier within Na layers. As a consequence, this phase transition free P2-NLNMO material delivers a high specific capacity of  $123 \text{ mA h g}^{-1}$  at 0.1 C with a high average voltage of 3.5 V, excellent rate capability ( $79.3 \text{ mA h g}^{-1}$  at 20 C), and ultra-stable cycle capability (85.4% capacity retention after 500 cycles at 5 C).

## Results and Discussion

### Crystal Structures of P2-NNMO and P2-NLNMO

P2-NNMO and P2-NLNMO were prepared through a feasible solid-state reaction. The synthesis details are presented in Experimental Section in the Supporting Information. The stoichiometry of the prepared compounds was confirmed by inductively coupled plasma atomic emission spectroscopy (ICP-AES), as indicated in Table S1 (see the Supporting Information), which are in good agreement with the ratios of reactants. Figures 1a and b show the X-ray diffraction (XRD) and Rietveld refinement patterns of P2-

NNMO and P2-NLNMO, respectively. All the diffraction peaks can be well indexed to a typical P2 phase with the  $P6_3/mmc$  space group. The XRD Rietveld refinement patterns demonstrate Li, Ni, and Mn atoms are all located within the transition-metal layer, occupying the octahedral 2a sites. There are two different prismatic sites in the Na layer. One is the edge-sharing site ( $\text{Na}_e$ ), and the other is face sharing with adjacent oxide layers ( $\text{Na}_f$ ). A preferred occupancy at  $\text{Na}_e$  sites is observed because of lower electrostatic repulsion at this position, which is commonly observed in P2-type compounds.<sup>[10a,11a,14]</sup> The specific crystallographic data of P2-NNMO and P2-NLNMO are listed in Tables S2 and S3, respectively. In theory, when the off-stoichiometry of Na in  $\text{Na}_x\text{MO}_2$  (typically  $x > 0.8$ ) is synthesized, the O3-type phase is experimentally to be structurally stabilized. To further understand the mechanism why the P2-NLNMO is formed when the off-stoichiometry of Na is 0.85, the formation energy ( $E_{\text{form}}$ ) of P2/O3-NLNMO were calculated using density functional theory (DFT) calculation. As depicted in Figure 1c, the formation energy of P2-NLNMO (−206.49 eV) is less than O3-NLNMO (−155.64 eV). Therefore, the P2-NLNMO structure is thermodynamically more stable than O3-NLNMO phase at this composition. The morphologies of prepared P2-NNMO and P2-NLNMO samples are characterized by scanning electron microscopy (SEM) and transmission electron microscopy (TEM). The P2-NLNMO possesses a plate-like morphology with the particle size of about 1–5  $\mu\text{m}$ . (Figure 1d, e). The high-resolution TEM (HRTEM) image in Figure 1f reveals the clear lattice fringe with a space of 5.6 Å, which matches well with the (002) plane of hexagonal P2-NLNMO. The SEM and HRTEM images (see Figure S1) of P2-NNMO are similar to those of P2-NLNMO because of their same space group with  $P6_3/mmc$ . Selected area electron diffraction (SAED) was conducted to obtain the specific structural information of P2-NLNMO. The bright spots could be well indexed to the representative reflections based on the P2 layered structure viewed along the [001] zone, as shown in Figure 1g. Figure 1h shows the energy-dispersive spectroscopy (EDS) mapping images of P2-NLNMO, which indicate that the elements of Na, Ni, Mn, and O are uniformly distributed in P2-NLNMO.

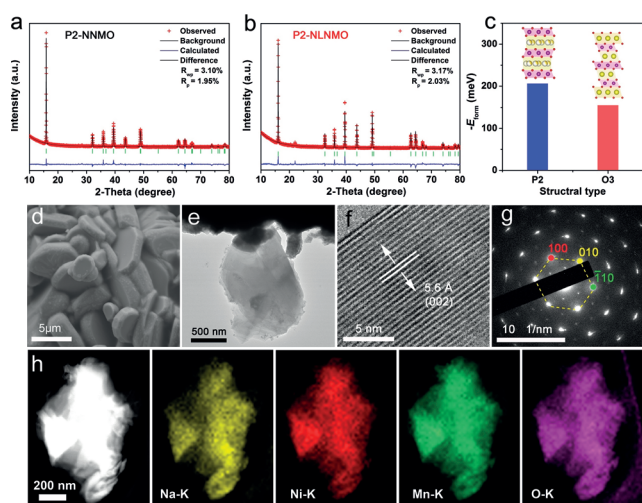


**Figure 1.** Structure of P2-NNMO and P2-NLNMO materials. XRD and Rietveld plots of a) P2-NNMO and b) P2-NLNMO. c) The energy formation ( $E_{\text{form}}$ ) for P2/O3-NLNMO. d) SEM, e) TEM, f) HRTEM, g) SAED pattern, and h) TEM (HAADF Na Ni Mn O) elemental mapping images of P2-NLNMO.

### Electrochemical Performance

The battery performance of P2-NNMO and P2-NLNMO cathodes were tested in Na half cells in a wide voltage range of 2.0–4.3 V (vs.  $\text{Na}^+/\text{Na}$ ). The theoretical capacity of P2-NNMO ( $1 \text{ C} = 211 \text{ mA h g}^{-1}$ ) and P2-NLNMO ( $1 \text{ C} = 224 \text{ mA h g}^{-1}$ ) in this paper are based on assuming all the  $\text{Na}^+$  extract from the materials. Figures 2a and b show the typical charge/discharge curves of P2-NNMO and P2-NLNMO, respectively, at a current density of 0.1 C during the first five cycles. Their corresponding cyclic voltammogram (CV) curves are presented in Figure S2. The charge/discharge curves of P2-NNMO show several voltage plateaus. The plateaus below 4.0 V are ascribed to the different  $\text{Na}^+/\text{vacancy}$  ordering rearrangement, and the plateau beyond 4.0 V corresponds to the phase transition from P2 to O2.<sup>[9b,15]</sup>



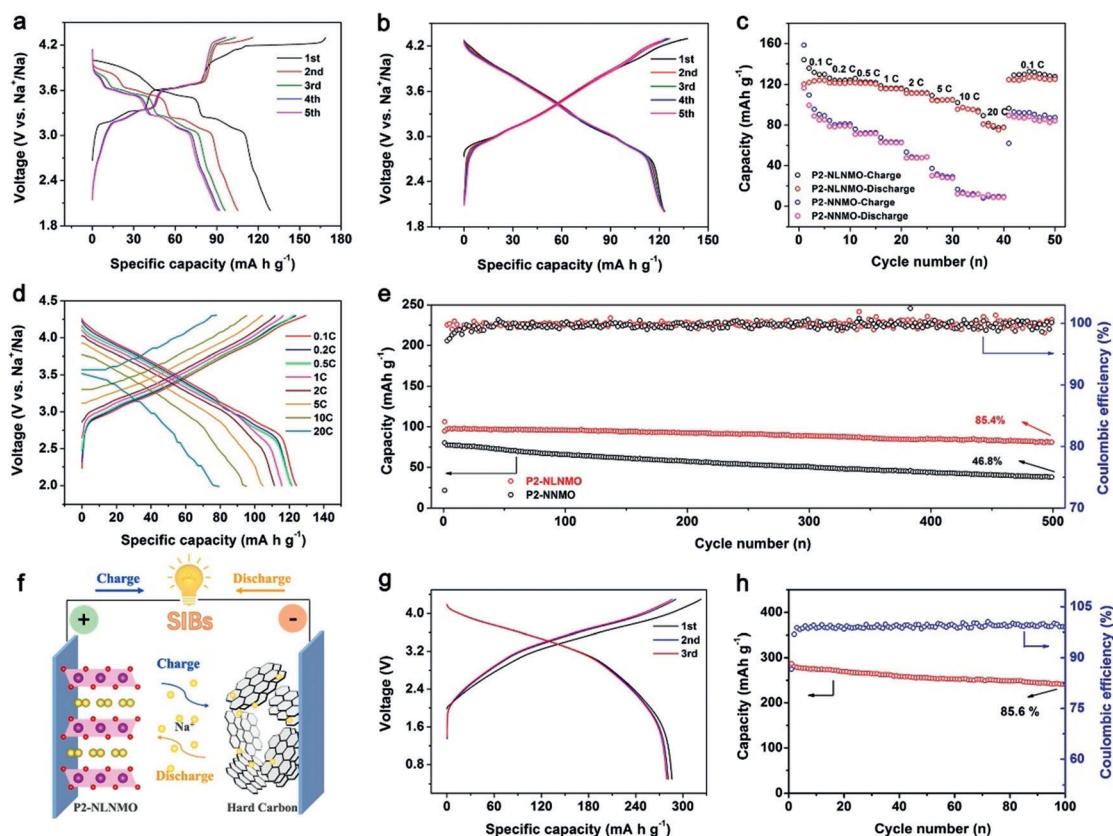


**Figure 2.** Electrochemical performance of P2-NNMO and P2-NLNMO compounds in Na cells. Galvanostatic charge/discharge curves of a) P2-NNMO and b) P2-NLNMO at 0.1 C in the voltage range of 2.0–4.3 V. c) Rate performance comparison of P2-NNMO and P2-NLNMO at different rates. d) Galvanostatic charge/discharge curves of P2-NLNMO at different rates in the voltage range of 2.0–4.3 V. e) Cycling performance of P2-NNMO and P2-NLNMO at 5 C. f) Schematic illustrating the charge/discharge process of full cell coupling P2-NLNMO as cathode and hard carbon as anode. g) Galvanostatic charge/discharge curves of full cell at 0.2 C. h) Cycling performance of full cell during 100 cycles at 0.2 C.

The CV behavior of the P2-NLNMO electrode indeed resembles that of capacitors, which is caused by Na-vacancy transitions changing from ordering to disordering after Li substitution. As shown in Figure S3, there are two possible oxygen layer migration directions during the transition process from P2 to O2, the random gliding of the oxygen layers may cause the lattice mismatch and dislocations.<sup>[11a]</sup> The resulting lattice disorder can break the active particles and further degrade cycle performance.<sup>[16]</sup> Therefore, P2-NNMO suffers from rapid capacity decay in the first several cycles, especially in the voltage range beyond 4.0 V. Whereas P2-NLNMO delivered a high and stable discharge capacity of 123.4 mA h g<sup>-1</sup>, as depicted in Figure 2b. The charge/discharge profiles of P2-NLNMO are sloping lines, even at potentials above 4.3 V, indicating P2→O2 transition above 4.3 V is completely suppressed. When charged to 4.5 V, a long voltage plateau in the charge and discharge curves (see Figure S4a) come from the anionic redox. An obvious peak near 4.4 V in the dQ/dV curves (see Figure S4b) further confirm the O<sup>2-</sup>/(O<sub>2</sub>)<sup>n-</sup> redox couple. Figure S5 shows the projected density of states (DOS) and electronic structure of P2-NLNMO. It can be found that Ni 3d, Mn 3d, and O 2p are hybridized near Fermi level, indicating that oxygen might participate in the electrochemical reaction in the high voltage region.<sup>[17]</sup> P2-NLNMO also shows much better rate perfor-

mance than P2-NNMO as demonstrated in Figure 2c. Figure 2d display the corresponding charge/discharge curves of P2-NLNMO at different rates. P2-NLNMO delivers reversible discharge capacities of 123.4, 121.9, 121.2, 115.8, 111.4, 104.8, 95.8, and 79.3 mA h g<sup>-1</sup> at 0.1, 0.2, 0.5, 1, 2, 5, 10, and 20 C, respectively, while the P2-NNMO electrode exhibits much inferior rate performance, with only 8.8 mA h g<sup>-1</sup> at 20 C. The superior rate performance of P2-NLNMO may be ascribed to the solid-solution reaction mechanism with fast Na<sup>+</sup> kinetics.<sup>[18]</sup> Na<sup>+</sup> mobility in P2-NLNMO will be discussed in detail in the latter parts. The cycling performance of P2-NNMO and P2-NLNMO at 0.1 C and 5 C are shown in Figure S6 and Figure 2e, respectively. P2-NLNMO exhibits a high capacity retention with 90.4 % at 0.1 C after 100 cycles, and 85.4 % capacity retention at 5 C after 500 cycles. While P2-NNMO encounters very fast capacity decay no matter in 0.1 C or 5 C. Another critical challenge for layered Na layered oxides is the poor air/water stability, which increases battery production and transportation costs.<sup>[3a]</sup> Surprisingly, the XRD patterns of P2-NLNMO shows no change after air/water treatment (see Figure S7), demonstrating the super structural stability resulting from the strong coupling interactions between adjacent TMO<sub>2</sub> sheets. Furthermore, the electrochemical performance of P2-NLNMO did not show obvious degradation after air/water treatment (see Figure S8). The



outstanding air/water stability of P2-NLNMO greatly increase its application prospect. We also compared the electrochemical performance of P2-NLNMO with typical Ni/Mn-based P2-type Na layered oxides in the literature.<sup>[9a, 10, 11b, 12, 13b]</sup> Because of the solid-solution reaction mechanism, Na<sup>+</sup>/vacancy disordering, and high Na content, the electrochemical performance of P2-NLNMO outperforms almost all the previously reported Ni/Mn-based sodium layered oxides (see Table S4) and typical cathodes (see Table S5) for SIBs. By coupling with a hard carbon (HC) anode, a P2-NLNMO/HC full cell was assembled (Figure 2f). Hard carbon was pre-cycled before used in full cell owing to its low Columbic efficiency in first cycle. The typical discharge/charge curves of hard carbon in first three cycles are displayed in Figure S9. The P2-NLNMO/HC full cell delivers a high reversible capacity of about 286 mAh g<sup>-1</sup> at 0.2 C with a high average operation voltage of about 3.4 V, based on the mass of anode material (Figure 2g). Moreover, the full cell exhibits the excellent cycling performance with 85.6% capacity retention after 100 cycles (Figure 2h).

### Structural Evolution and Reaction Mechanism

To further understand the structural evolution of P2-NLNMO during Na<sup>+</sup> ions extraction and insertion, we performed in situ XRD between 2.0 and 4.3 V during the first charge/discharge cycle (Figure 3a). Corresponding intensity contour maps are shown in Figure 3b. As sodium ions are removed, the (100), (102), and (103) diffraction lines shift toward a higher angle because of contracted *ab* plane and smaller ionic radius by electrochemical oxidation. Meanwhile, (002) and (004) peaks of P2-NLNMO show clear shift to lower angle, indicating that the *c* axis is expanding owing to enlarged electrostatic repulsion between neighboring oxygen layers. During the discharge process, all these shifted diffraction peaks return to their original positions, demonstrating the highly reversible sodium storage behavior in P2-NLNMO. Note that there was no new phase formation or

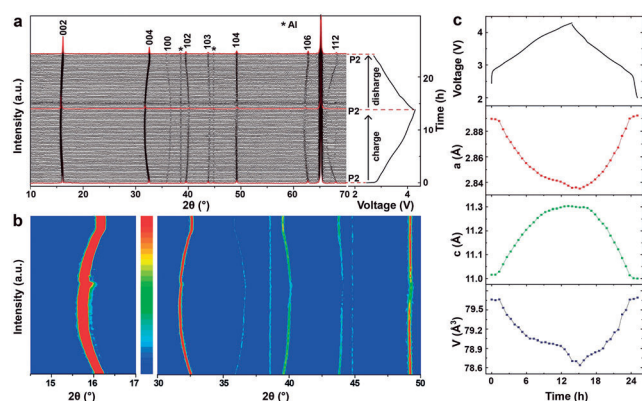


**Figure 3.** Crystal structural evolution of P2-NLNMO upon Na<sup>+</sup> extraction/insertion. a) In-situ XRD patterns collected during the first charge/discharge of the P2-NLNMO electrode cycled at 0.1 C between 2.0 and 4.3 V. b) Contour map of in situ XRD patterns for P2-NLNMO. c) The variation of lattice constants and unit-cell volume along with sodium ions extraction and insertion for P2-NLNMO.

phase transition during the whole charge/discharge process, demonstrating a complete solid-solution behavior in P2-NLNMO. The solid-solution behavior is also reflected in the continuous change of lattice constants (*a* and *c*) and unit-cell volume (*V*) of P2-NLNMO at different states of sodium extraction and insertion (Figure 3c). The change law of *a* and *c* axis are in accordance with the shift of (10*l*) and (00*l*) diffraction lines by in situ XRD patterns. Moreover, volume change of the unit cell caused before and after Na<sup>+</sup> extraction in P2-NLNMO is only 1.7%. Such a low cell volume change is nearly zero strain because of the complete elimination of P2→OP4/O2 transition, as the volume changes for P2 transform to OP4/O2 are reported to be 13% and 23%, respectively.<sup>[6b]</sup> Therefore, partial Li substitution for Ni/Mn with compatible ionic radii and very different Fermi levels in P2-NNMO effectively prevents Na<sup>+</sup>/vacancy ordering and eliminates phase transformations during cycling, thus extending the complete solid solution zone over a wider Na intercalation range. Such a low volume change in the total solid-solution pathway significantly enhances both the rate performance and cycling stability.

### Charge Compensation During Charge/Discharge

To elucidate the charge compensation mechanism of P2-NLNMO upon Na<sup>+</sup> (de)intercalation, ex situ X-ray absorption structure spectroscopy (XAS) measurements were carried out. The normalized X-ray absorption near-edge structure (XANES) spectra of Ni and Mn K-edge were collected at different charge/discharge states, which are shown in Figure 4a and b, respectively. After charging to 4.3 V, the Ni K-edge adsorption spectrum of P2-NLNMO (Figure 4a) obviously shifts about 3 eV toward the high-energy value, indicating the oxidation of Ni<sup>2+</sup> to Ni<sup>4+</sup>,<sup>[19]</sup> while the Mn K-edge adsorption spectra (Figure 4b) show no change during electrochemical oxidation and reduction, demonstrating the

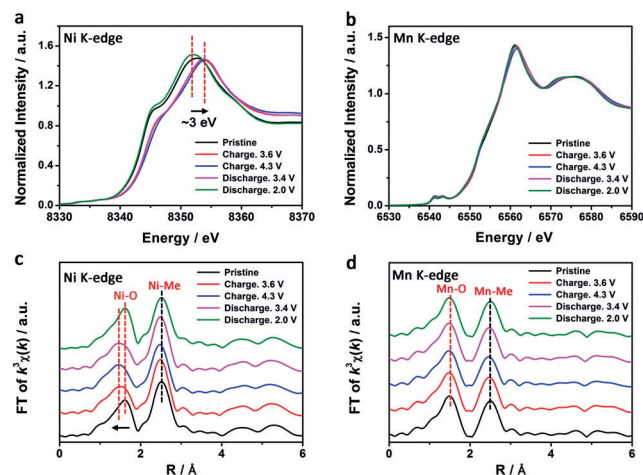


**Figure 4.** Charge compensation mechanism of P2-NLNMO upon Na<sup>+</sup> extraction/insertion. Ex situ XANES spectra at the a) Ni K-edge and b) Mn K-edge of P2-NLNMO electrode collected at different charge/discharge states. Ex situ EXAFS spectra at the c) Ni K-edge and d) Mn K-edge of P2-NLNMO electrode collected at different charge/discharge states. FT = Fourier transform.



electrochemically inactive of  $\text{Mn}^{4+}$  in P2-NLNMO. The interatomic distances of P2-NLNMO were further investigated by extended X-ray absorption fine structure (EXAFS) spectra at Ni and Mn K-edges, as displayed in Figure 4c and d, respectively. In the first Ni-O coordination shell of P2-NLNMO, a shortened interatomic distance and a lowered Fourier transform (FT) magnitude were observed at the Ni K-edge for compensating the charge balance. While there is no obvious change at the Mn K-edge upon  $\text{Na}^+$  removal and the Mn ions still maintain the tetravalence. The EXAFS results agree well with the XANES and Ab initio molecular dynamics (AIMD) simulations results (see Figure S10 and Table S6). Consistent with the change law of lattice parameter  $a$  as revealed by in situ XRD results, both Ni and Mn K-edges deliver a slight shift toward lower in-plane interatomic distances upon sodium extraction from crystal lattice in the TM-TM second coordination shells.

### $\text{Na}^+$ Kinetics and Reaction Mechanism Study

To further probe the  $\text{Na}^+$  kinetics difference in solid solution (single-phase) and multiphase reactions, galvanostatic intermittent titration techniques (GITT) were performed for the P2-NNMO and P2-NLNMO samples. Three pairs of obvious voltage platforms are observed in GITT curve of P2-NNMO (Figure 5a), indicating a typical multiphase reaction. The equilibrium voltage of P2-NLNMO in GITT curve (Figure 5b) presents a consecutive variation, suggesting the solid-solution pathway upon sodium insertion and extraction. According to the GITT data, the calculated diffusion coefficient of Na ions ( $D_{\text{Na}^+}$ ) in P2-NNMO and P2-NLNMO are displayed in Figure 5c. The  $D_{\text{Na}^+}$  value determined by GITT for P2-NLNMO is approximately  $10^{-11}$  to  $10^{-10} \text{ cm}^2 \text{ s}^{-1}$ , which is two orders of magnitude higher than  $D_{\text{Na}^+}$  in P2-NNMO ( $10^{-13}$  to  $10^{-12} \text{ cm}^2 \text{ s}^{-1}$ ). With the help of

DFT calculation, the formation energy ( $E_{\text{form}}$ ) of inter-species upon  $\text{Na}^+$  extraction was calculated to confirm the single-phase pathway, as shown in Figure 5d. It can be clearly found that the formation energies of the P2 phase are always lower than that of O2 phase during Na exaction, indicating that P2 is the thermodynamically stable phase during the whole electrochemical process. This result also provides a theoretical basis for the solid solution reaction mechanism in P2-NLNMO. Ab initio molecular dynamics (AIMD) simulations have further been conducted to study the  $\text{Na}^+$  transport property in P2-NLNMO. The mean square displacements (MSD) of sodium ions for  $\text{P2-Na}_{0.83}\text{Li}_{0.13}\text{Ni}_{0.21}\text{Mn}_{0.67}\text{O}_2$  at the corresponding temperatures are presented in Figure S11. As shown in Figure 5e,  $\text{Na}^+$  ions in P2-NLNMO migrates through 2D diffusion pathway, which can facilitate the  $\text{Na}^+$  diffusion kinetics and agree with the characteristics of layered transition metal oxides. The corresponding vertical view of trajectories within single Na layer are displayed in the right side of Figure 5e, suggesting an ideal  $\text{Na}_i\text{-Na}_e\text{-Na}_f$  diffusion pathway. Additionally, the AIMD simulations performed at different temperatures (700, 800, 900 K) are used to obtain the diffusion energy barrier ( $E_a$ ). The diffusion coefficient ( $D$ ) can be obtained by fitting the MSD time curves. Then, the diffusion energy barrier was calculated to be 320 meV based on the slope of Arrhenius plot, as depicted in Figure 5f. This value of diffusion energy barrier for P2-NLNMO is relatively low, matching well with the experimental GITT result.

### Conclusion

In summary, the priority of the solid-solution region over the two-phase reaction/Na-vacancy ordering is demonstrated in a high sodium content P2-type  $\text{Na}_{0.85}\text{Li}_{0.12}\text{Ni}_{0.22}\text{Mn}_{0.66}\text{O}_2$  cathode. In situ XRD shows both  $\text{P2} \rightarrow \text{O2}/\text{OP4}$  phase transitions and  $\text{Na}^+$ /vacancy ordering can be successfully

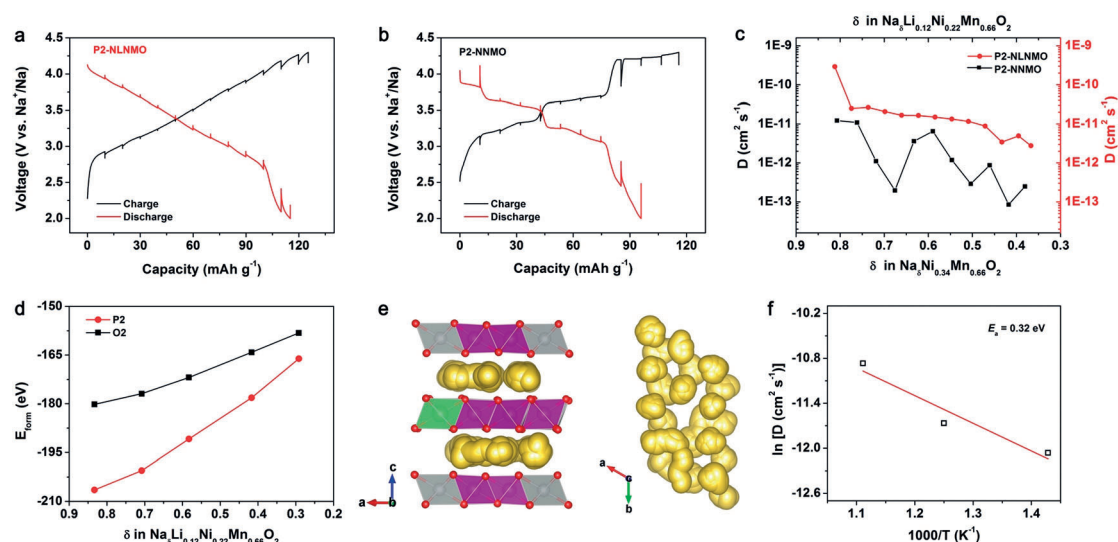


**Figure 5.**  $\text{Na}^+$  kinetics and reaction mechanism study of P2-NLNMO. GITT curves of a) P2-NLNMO and b) P2-NNMO electrodes. c) Calculated Na chemical diffusion coefficients of P2-NLNMO and P2-NNMO electrodes from GITT. d) The formation energy of P2-NLNMO at different Na concentrations. e) Trajectories of  $\text{Na}^+$  in P2-NLNMO simulated at a temperature of 800 K. The top view of each  $\text{Na}^+$  layer is given in the right panel. f) Arrhenius plot of  $\text{Na}^+$  diffusion coefficients.



converted into a complete solid solution dominated region after Li substitution. Owing to the simplified phase boundaries for Na transport, the resulting fast Na diffusion ( $10^{-11}$  to  $10^{-10}$  cm<sup>2</sup>s<sup>-1</sup>) and low diffusion barrier (320 meV) are acquired by the combined analysis of GITT and molecular dynamic simulation. As a result, the P2-NLNMO compound having sufficient sodium content could deliver a large specific capacity of 123 mA h g<sup>-1</sup> with average working voltage as high as 3.5 V, and totally smooth charge and discharge curves free from voltage plateau, which contribute to the superior rate capability (79.3 mA h g<sup>-1</sup> at 20 °C) and ultrastable cycle performance (85.4% capacity retention after 500 cycles at 5 °C). This work highlights the importance of the solid-solution reaction mechanism in a high sodium content P2-type cathode, which ensures the both superior cycling stability with small volume variation and remarkable rate capability with good Na<sup>+</sup> kinetics.

## Acknowledgements

This work was financially supported by the National Natural Science Foundation of China (51622102, 21421001, 21835004), Ministry of Science and Technology of China (2017YFA0206702, 2016YFB0901502), the 111 Project (B12015), Natural Science Foundation of Tianjin (18ZXJMTG00040, 19JCZDJC31800). T.J.'s fellowship was supported by China Scholarship Council (Grant No. 201806200071). Q.C.W. and X.-Q.Y. were supported by the Assistant Secretary for Energy Efficiency and Renewable Energy, Vehicle Technology Office of the US Department of Energy through the Advanced Battery Materials Research Program under contract DE-SC0012.

## Conflict of interest

The authors declare no conflict of interest.

- [1] a) M. Armand, J.-M. Tarascon, *Nature* **2008**, *451*, 652–657; b) D. Kundu, E. Talaie, V. Duffort, L. F. Nazar, *Angew. Chem. Int. Ed.* **2015**, *54*, 3431–3448; *Angew. Chem.* **2015**, *127*, 3495–3513; c) Y. Lu, X. Hou, L. Miao, L. Li, R. Shi, L. Liu, J. Chen, *Angew. Chem. Int. Ed.* **2019**, *58*, 7020–7024; *Angew. Chem.* **2019**, *131*, 7094–7098; d) T. Jin, Q. Han, L. Jiao, *Adv. Mater.* **2020**, *32*, 1806304; e) Y. Qi, Y. Lu, F. Ding, Q. Zhang, H. Li, X. Huang, L. Chen, Y.-S. Hu, *Angew. Chem. Int. Ed.* **2019**, *58*, 4361–4365; *Angew. Chem.* **2019**, *131*, 4405–4409.
- [2] a) K. Kubota, S. Kumakura, Y. Yoda, K. Kuroki, S. Komaba, *Adv. Energy Mater.* **2018**, *8*, 1703415; b) T. Jin, Q. Han, Y. Wang, L. Jiao, *Small* **2018**, *14*, 1703086; c) P. K. Nayak, L. Yang, W. Brehm, P. Adelhelm, *Angew. Chem. Int. Ed.* **2018**, *57*, 102–120; *Angew. Chem.* **2018**, *130*, 106–126; d) N. Yabuuchi, K. Kubota, M. Dahbi, S. Komaba, *Chem. Rev.* **2014**, *114*, 11636–11682.
- [3] a) P.-F. Wang, Y. You, Y.-X. Yin, Y.-G. Guo, *Adv. Energy Mater.* **2018**, *8*, 1701912; b) X. D. Xiang, K. Zhang, J. Chen, *Adv. Mater.* **2015**, *27*, 5343–5364; c) Y. Xiao, Y. F. Zhu, W. Xiang, Z. G. Wu, Y. C. Li, J. Lai, S. Li, E. H. Wang, Z. G. Yang, C. L. Xu, B. H. Zhong, X. Guo, *Angew. Chem. Int. Ed.* **2020**, *59*, 1491–1495; *Angew. Chem.* **2020**, *132*, 1507–1511; d) Z. Yan, L. Tang, Y. Huang, W. Hua, Y. Wang, R. Liu, Q. Gu, S. Indris, S. L. Chou, Y. Huang, M. Wu, S. X. Dou, *Angew. Chem. Int. Ed.* **2019**, *58*, 1412–1416; *Angew. Chem.* **2019**, *131*, 1426–1430; e) C. Zhao, M. Avdeev, L. Chen, Y. S. Hu, *Angew. Chem. Int. Ed.* **2018**, *57*, 7056–7060; *Angew. Chem.* **2018**, *130*, 7174–7178; f) C. Zhao, F. Ding, Y. Lu, L. Chen, Y. S. Hu, *Angew. Chem. Int. Ed.* **2020**, *59*, 264–269; *Angew. Chem.* **2020**, *132*, 270–275.
- [4] C. Delmas, C. Fouassier, P. Hagenmuller, *Physica* **1980**, *99B*, 81–85.
- [5] a) R. J. Clément, P. G. Bruce, C. P. Grey, *J. Electrochem. Soc.* **2015**, *162*, A2589–A2604; b) K. Kubota, S. Komaba, *J. Electrochem. Soc.* **2015**, *162*, A2538–A2550.
- [6] a) Z. Lu, J. R. Dahn, *J. Electrochem. Soc.* **2001**, *148*, A1225–A1229; b) N. Yabuuchi, R. Hara, M. Kajiyama, K. Kubota, T. Ishigaki, A. Hoshikawa, S. Komaba, *Adv. Energy Mater.* **2014**, *4*, 1301453.
- [7] D. H. Lee, J. Xu, Y. S. Meng, *Phys. Chem. Chem. Phys.* **2013**, *15*, 3304–3312.
- [8] Y. Wang, R. Xiao, Y. S. Hu, M. Avdeev, L. Chen, *Nat. Commun.* **2015**, *6*, 6954.
- [9] a) P. F. Wang, Y. You, Y. X. Yin, Y. S. Wang, L. J. Wan, L. Gu, Y. G. Guo, *Angew. Chem. Int. Ed.* **2016**, *55*, 7445–7449; *Angew. Chem.* **2016**, *128*, 7571–7575; b) G. Singh, N. Tapia-Ruiz, J. M. Lopez del Amo, U. Maitra, J. W. Somerville, A. R. Armstrong, J. Martinez de Ilarduya, T. Rojo, P. G. Bruce, *Chem. Mater.* **2016**, *28*, 5087–5094.
- [10] a) P. F. Wang, H. R. Yao, X. Y. Liu, Y. X. Yin, J. N. Zhang, Y. Wen, X. Yu, L. Gu, Y. G. Guo, *Sci. Adv.* **2018**, *4*, eaar6018; b) H. Yoshida, N. Yabuuchi, K. Kubota, I. Ikeuchi, A. Garsuch, M. Schulz-Dobrick, S. Komaba, *Chem. Commun.* **2014**, *50*, 3677–3680.
- [11] a) L. Yang, X. Li, J. Liu, S. Xiong, X. Ma, P. Liu, J. Bai, W. Xu, Y. Tang, Y. Y. Hu, M. Liu, H. Chen, *J. Am. Chem. Soc.* **2019**, *141*, 6680–6689; b) J. Xu, D. H. Lee, R. J. Clément, X. Yu, M. Leskes, A. J. Pell, G. Pintacuda, X.-Q. Yang, C. P. Grey, Y. S. Meng, *Chem. Mater.* **2014**, *26*, 1260–1269; c) D. Kim, S.-H. Kang, M. Slater, S. Rood, J. T. Vaughan, N. Karan, M. Balasubramanian, C. S. Johnson, *Adv. Energy Mater.* **2011**, *1*, 333–336.
- [12] X. Wu, J. Guo, D. Wang, G. Zhong, M. J. McDonald, Y. Yang, *J. Power Sources* **2015**, *281*, 18–26.
- [13] a) K. Kubota, Y. Yoda, S. Komaba, *J. Electrochem. Soc.* **2017**, *164*, A2368–A2373; b) L. Zheng, J. Li, M. N. Obrovac, *Chem. Mater.* **2017**, *29*, 1623–1631.
- [14] W. M. Dose, N. Sharma, J. C. Pramudita, J. A. Kimpton, E. Gonzalo, M. H. Han, T. Rojo, *Chem. Mater.* **2016**, *28*, 6342–6354.
- [15] C. Zhao, Y. Lu, L. Chen, Y.-S. Hu, *Nano Res.* **2019**, *12*, 2018–2030.
- [16] a) M. D. Radin, A. Van der Ven, *Chem. Mater.* **2018**, *30*, 607–618; b) M. D. Radin, J. Alvarado, Y. S. Meng, A. Van der Ven, *Nano Lett.* **2017**, *17*, 7789–7795.
- [17] a) R. A. House, U. Maitra, M. A. Pérez-Osorio, J. G. Lozano, L. Jin, J. W. Somerville, L. C. Duda, A. Nag, A. Walters, K.-J. Zhou, M. R. Roberts, P. G. Bruce, *Nature* **2020**, *577*, 502–508; b) X. Rong, E. Hu, Y. Lu, F. Meng, C. Zhao, X. Wang, Q. Zhang, X. Yu, L. Gu, Y.-S. Hu, H. Li, X. Huang, X.-Q. Yang, C. Delmas, L. Chen, *Joule* **2019**, *3*, 503–517; c) X. Rong, J. Liu, E. Hu, Y. Liu, Y. Wang, J. Wu, X. Yu, K. Page, Y.-S. Hu, W. Yang, H. Li, X.-Q. Yang, L. Chen, X. Huang, *Joule* **2018**, *2*, 125–140.
- [18] S. Atlung, K. West, T. Jacobsen, *J. Electrochem. Soc.* **1979**, *126*, 1311–1321.
- [19] W.-S. Yoon, S. Iannopollo, C. P. Grey, D. Carlier, J. Gorman, J. Reed, G. Ceder, *Electrochem. Solid-State Lett.* **2004**, *7*, A167–A171.

Manuscript received: March 17, 2020

Revised manuscript received: May 31, 2020

Accepted manuscript online: June 5, 2020

Version of record online: ■ ■ ■ ■ ■ ■ ■ ■ ■ ■

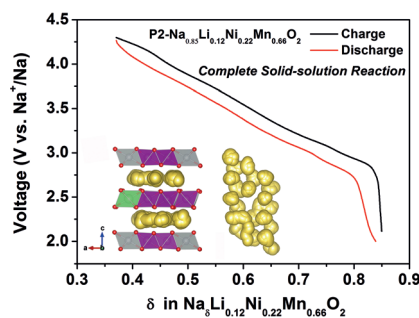
## Research Articles



## Electrochemistry

T. Jin, P.-F. Wang, Q.-C. Wang, K. Zhu,  
T. Deng, J. Zhang, W. Zhang, X.-Q. Yang,  
L. Jiao,\* C. Wang\* ——— ■■■■—■■■■

Realizing Complete Solid-Solution  
Reaction in High Sodium Content P2-  
Type Cathode for High-Performance  
Sodium-Ion Batteries



**A high sodium content (0.85) and plateau-free P2-type cathode,**  $\text{Na}_{0.85}\text{Li}_{0.12}\text{Ni}_{0.22}\text{Mn}_{0.66}\text{O}_2$ , is developed for sodium-ion batteries. The sodium content promises a large specific capacity of  $123.4 \text{ mAh g}^{-1}$  with an average working voltage as high as 3.5 V. The complete solid-solution reaction over a wide voltage range ensures small volume variation (1.7%) and fast  $\text{Na}^+$  kinetics ( $10^{-10}$  to  $10^{-11} \text{ cm}^2 \text{ s}^{-1}$ ), contributing to both excellent cycling stability and rate capability.

